Modelling of membrane bonding response
Part 1 development of an adhesive contact interface element

Liu, Xueyan; Kasbergen, Cor; Li, Jinlong; Scarpas, Tom

DOI
10.1080/10298436.2020.1763992

Publication date
2020

Document Version
Final published version

Published in
International Journal of Pavement Engineering

International Journal of Pavement Engineering

ISSN: (Print) (Online) Journal homepage: https://www.tandfonline.com/loi/gpav20

Modelling of membrane bonding response: part 1 development of an adhesive contact interface element

Xueyan Liu, Cor Kasbergen, Jinlong Li & Tom Scarpas

To cite this article: Xueyan Liu, Cor Kasbergen, Jinlong Li & Tom Scarpas (2022) Modelling of membrane bonding response: part 1 development of an adhesive contact interface element, International Journal of Pavement Engineering, 23:3, 612-625, DOI: 10.1080/10298436.2020.1763992

To link to this article: https://doi.org/10.1080/10298436.2020.1763992

Published online: 18 May 2020.

INTERNATIONAL JOURNAL OF PAVEMENT ENGINEERING
2022, VOL. 23, NO. 3, 612–625
https://doi.org/10.1080/10298436.2020.1763992

Modelling of membrane bonding response: part 1 development of an adhesive contact interface element

Xueyan Liu, Cor Kasbergen, Jinlong Li and Tom Scarpas

Section of Pavement Engineering, Faculty of Civil Engineering & Geosciences, Delft University of Technology, Delft, Netherlands

ABSTRACT

The adhesive bonding strength of the membrane layers between the asphalt concrete surface layers and the decks of steel bridges has a strong influence on the fatigue life of orthotropic steel deck bridges (OSDBs). The most important requirement for the application of membrane materials to orthotropic steel deck bridges is that the membrane adhesive layer is able to sufficiently bond to its surrounding material layers. The interfacial properties between the membrane and the layers bonded to it have not been extensively studied in the current orthotropic steel deck bridge system. In this paper, details of the contact interface element utilised to model the interfacial bonding properties will be discussed. Furthermore, the traction-separation material law will be chosen to describe the bonding response of the interfacial properties of the membrane to its surrounding surfacing layers on OSDBs. Some numerical examples, in which various aspects of the finite elements response of the contact interface model will be presented. Utilisation of the model in finite element analyses has enabled the investigation of the response of a 3D orthotropic steel deck bridge subjected to the different traffic loading conditions.

ARTICLE HISTORY
Received 23 May 2019
Accepted 27 April 2020

KEYWORDS
Adhesive bonding strength; contact interface element; membrane; asphalt concrete; orthotropic steel deck bridges; constitutive model; finite element

1. Introduction

Orthotropic steel deck bridges (OSDBs) are widely used in most of the major long-span bridges around the world. The lightweight and flexibility make OSDB a cost-effective solution for cases where a high degree of pre-fabrication or rapid erection is required, such as in seismic zones, for movable bridges, long-span bridges and for rehabilitation to reduce bridge weight.

In the Netherlands, an asphaltic surfacing structure for OSDBs mostly consists of multi structural layers. The upper layer consists of Porous Asphalt (PA) because of reasons related to noise reduction. For the lower layer a choice between Mastic Asphalt (MA) or Guss Asphalt (GA), can be made. Mostly, various membrane layers are involved, functioning as a bonding layer, isolation layer as well as adhesion layer. Unfortunately, the service life of the current Dutch asphaltic surfacing structures on OSDBs is limited to an average of 5 years. Several problems were observed in relation to asphaltic surfacing materials on OSDBs such as raveling, cracking, loss of bond between the surfacing material and the steel plate, etc. The severity of the problems is increased by the considerable growth of traffic in terms of number of trucks, heavier wheel loads, wide-base tires, etc. The availability of innovative design methodologies and advanced durable surfacing materials on OSDBs become very urgent for Dutch road authority and will offer opportunities to mitigate material response degradation and fatigue-related problems in this type of structure contributing thus to a significant extension of the service life of Dutch OSDBs.

Previous investigations have shown that the adhesive strength of the membrane layers between the surface layers and the decks of steel bridges has a strong influence on the structural response of orthotropic steel bridge decks (Liu *et al.* 2008, 2013, Li 2015, Tzimiris 2017). The most important requirement for the application of membrane materials to orthotropic steel bridge decks is that the membrane adhesive layer is able to sufficiently bond to the surrounding materials.

According to engineering practices, experimental and numerical investigations, when traffic load is imposed on the surface of OSDBs, non-uniform displacement fields develop resulting in a variety of states of stress in the surfacing material. An example is shown in Figure 1, which shows the response of the structure to a dual-wheel load. It can be observed that, when a dual wheel load is applied onto a steel deck surfacing, transversal tensile deformations are observed at upper locations in the vicinity of the middle support of the bridge which creates negative moments as well as the lower parts of the surfacing layers under the wheel load (Liu *et al.* 2010, Medani *et al.* 2010). In the meantime, depending on the bonding strength between the layers, shear deformations are developed between the membrane and structural layers. The higher bonding strength of the membrane interfaces can improve the integrity of the surfacing system. The shear deformation in the asphalt surfacing layers close to the membranes can be increased significantly by using the poor-bonded membranes which will result in adhesive failure (debonding) at the interfaces. This necessitates the search for a more powerful computational tool for increased understanding of the complicated response of asphaltic surfacing on orthotropic steel deck bridges. The tool should incorporate more realistic material behaviour and more realistic elements representing the adhesive bonding

CONTACT Xueyan Liu x.liu@tudelft.nl

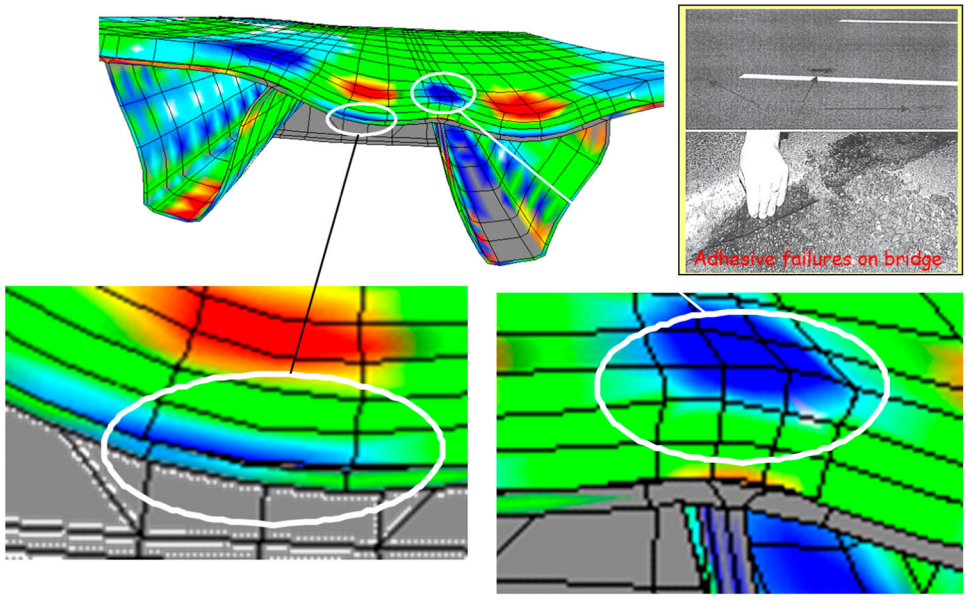

Figure 1. Contour of transversal stresses, deformation and adhesive failures of an orthotropic steel bridge under a dual wheel axle (red and blue colours indicate tensile and compressive stresses, respectively).

characteristics between the structural layers and the structural geometry.

The debonding process between two bodies is normally described by cohesive zone models which represent a relation between the traction and the relative displacement of associated points of crack surfaces. The tractions are sometimes coupled by making them a function of both the normal and tangential opening displacement (Tvergaard 1990, Xu and Needleman 1993). Cohesive zones are typically implemented in finite element codes as interface elements (Chandra *et al.* 2002, De Borst 2003, Van den Bosch *et al.* 2006).

In general, the membrane will either fail adhesively or cohesively. Cohesive failures are characterised by the fracture of the membrane in itself. Manufactures retain a relatively good understanding of their product properties and have been able to improve their physical properties over the years. This has led to the membrane with good cohesion properties, and thus rare cohesive failures. In contrast, the adhesive failure, a debonding near the membrane/asphalt concrete layers and membrane/steel deck plate is much more common (Medani *et al.* 2008). The interfacial properties between the membrane/asphalt concrete layers and membrane/steel deck plate have not been extensively studied in the orthotropic steel deck bridge system. The nature of adhesion is thus not very well understood. Furthermore, it is known that when the adhesion between the steel plate and the surfacing is lost, failure of the surfacing follows soon. This necessitates the search for a realistic representation of the behaviour of the interfacial properties of membrane material.

In order to gain insight into the mechanical response of membranes and their interaction with surrounding materials on orthotropic steel decks, a large project of experimental and computational investigation has been undertaken at Delft University of Technology. One of the primary goals of this investigation is the development of an appropriate adhesive constitutive interface model capable of describing the response of no-penetration, adhesive debonding, stick and frictional slippage between two objects. Once the model was available and verified, its implementation into the CAPA-3D finite element system (Scarpas 1992, Liu 2003, Liu *et al.* 2004) has enabled the simulation of the dynamic response of orthotropic steel deck bridges accounting for the effects of bonding effect between layers, material non-linearity, the complex geometry of orthotropic steel deck and moving load patterns.

In the first part of the paper, the details of the contact interface element will be discussed. Furthermore, an adhesive constitutive model for the proposed interface element will be presented. The traction-separation material law will be chosen to describe the bonding response of the interfacial properties of the membrane to its surrounding surfacing layers on OSDBs. Some numerical examples, in which various aspects of the finite elements response of the contact interface model will be presented. The importance of the interface (crack) opening and propagation in a double cantilever beam (DCB) specimen is used for description of the actual material layer debonding behaviour.

In a companion paper to this contribution, model predictions were compared with actual test data from membrane adhesion test (MAT). The progressive membrane debonding process of the MAT test was modelled by introducing the adhesive traction-separation element into the contact zone. Comparison of membrane deformation profiles and the in-time debonding force distribution between experimental observations and finite element simulations have been drawn. Availability of the adhesive constitutive interface model will allow in the future a better understanding of damage development at the membrane allowing thus optimisation of maintenance activities on OSDBs.

2. 3d interface finite element formulation

Normally, the bonding interface thickness of membrane with the surrounding surfacing layers on OSDBs is typically very

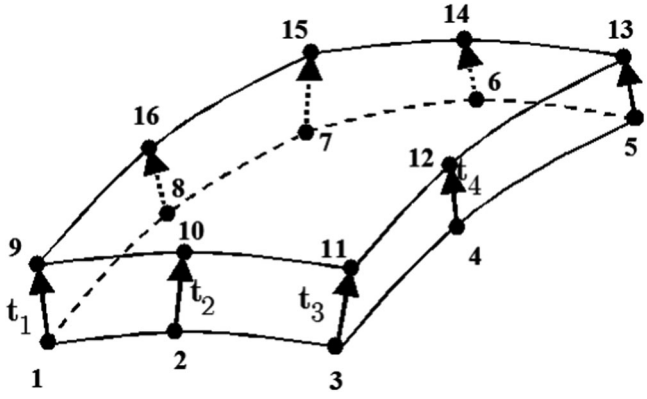

Figure 2. Schematic of a 3D interface element and local thickness vectors.

small in comparison to the lateral dimensions. In the context of the finite element method, the artifice of degenerating ordinary continuous finite elements into elements of very small thickness renders the elements grossly inaccurate. As a result, for adequate modelling of those systems, a special type of finite interface element needs to be developed.

In this paper, the development of an adhesive contact interface element implemented within the FE package CAPA-3D will be described. The element used in the FE simulation of the adhesive and contact behaviour of the membrane to the surrounding layers is achieved by means of a 16-noded isoparametric interface element, Figure 2. The element is compatible with the ordinary quadratic elements and can, therefore, be used in the modelling of thin layer and/or crack interface.

2.1. Element geometry interpolation

By utilising the element nodal coordinates, a mid-surface is defined as follows. For every pair of nodes, a local thickness vector is defined spanning from a node on the bottom surface of the element to the corresponding node on the top surface, Figure 3.

If the vector of nodal coordinates for a node k on the bottom surface of the element is defined as:

$$\mathbf{X}_k = \begin{bmatrix} X_{k1} & X_{k2} & X_{k3} \end{bmatrix}^T \tag{1}$$

then, the global coordinates of the middle point the corresponding local thickness vector can be computed as:

$$\begin{bmatrix} {}_mX_{k1} \\ {}_mX_{k2} \\ {}_mX_{k3} \end{bmatrix} = \begin{bmatrix} X_{k1} \\ X_{k2} \\ X_{k3} \end{bmatrix} + \frac{1}{2} \begin{bmatrix} t_{k1} \\ t_{k2} \\ t_{k3} \end{bmatrix} \qquad k = 1, \ldots 8 \tag{2}$$

As shown in Figure 3, at each middle point k, a unit local thickness vector $1\chi_k$ can be defined as:

$$\chi_{kj} = \frac{t_{kj}}{\|\mathbf{t}_k\|} \qquad j = 1, \ldots 3 \tag{3}$$

On the element middle surface, Figure 4, two curvilinear coordinate axes ξ_1 and ξ_2 are defined and a third linear axis ξ_3 that is locally perpendicular to the plane defined by ξ_1 and ξ_2. All axes span between $[-1, +1]$. The orientation of the axes is

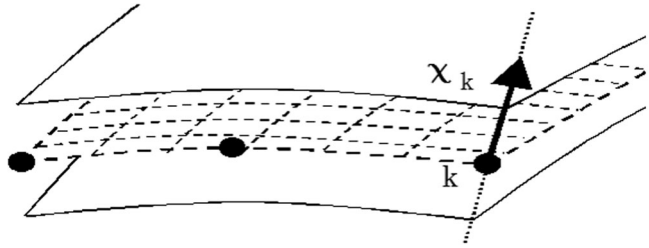

Figure 3. Local unit thickness vector definition.

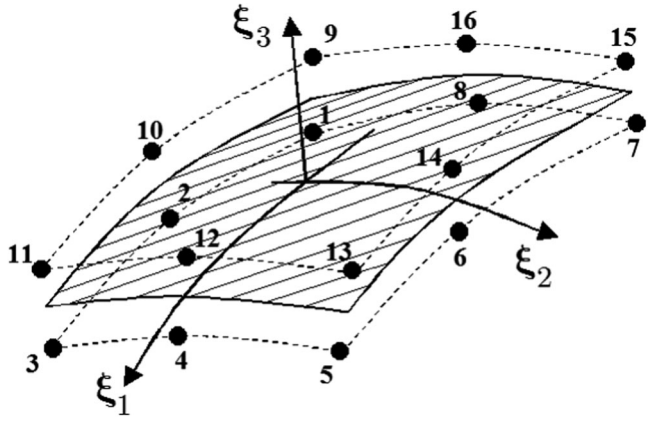

Figure 4. Curvilinear coordinate system.

determined by the local numbering of the bottom surface nodal points.

The global coordinates of any point within the element can be computed on the basis of the global coordinates of the middle surface defining points and the curvilinear coordinate system

$$\begin{bmatrix} X_1 \\ X_2 \\ X_3 \end{bmatrix} = \sum_{k=1}^{8} N_k \begin{bmatrix} {}_mX_{k1} \\ {}_mX_{k2} \\ {}_mX_{k3} \end{bmatrix} + \sum_{k=1}^{8} N_k \left(\frac{t_k}{2}\right) \xi_3 \begin{bmatrix} \chi_{k1} \\ \chi_{k2} \\ \chi_{k3} \end{bmatrix} \tag{4}$$

in which N_k are the standard 2-D shape functions

$$\begin{aligned} N_1 &= (1-\xi_1)(1-\xi_2)(-\xi_1-\xi_2-1)/4 \\ N_2 &= (1-\xi_1^2)(1-\xi_2)/2 \\ N_3 &= (1+\xi_1)(1-\xi_2)(+\xi_1-\xi_2-1)/4 \\ N_4 &= (1+\xi_1)(1-\xi_2^2)/2 \\ N_5 &= (1+\xi_1)(1+\xi_2)(+\xi_1+\xi_2-1)/4 \\ N_6 &= (1-\xi_1^2)(1+\xi_2)/2 \\ N_7 &= (1-\xi_1)(1+\xi_2)(-\xi_1+\xi_2-1)/4 \\ N_8 &= (1-\xi_1)(1-\xi_2^2)/2 \end{aligned} \tag{5}$$

2.2. Field variables interpolation

The local response of the contact region between two interacting surfaces can be described in terms of the relative motion of two points j and i, one on each of the surfaces. As shown in Figure 5 two relative slip displacements and a relative normal displacement can be defined.

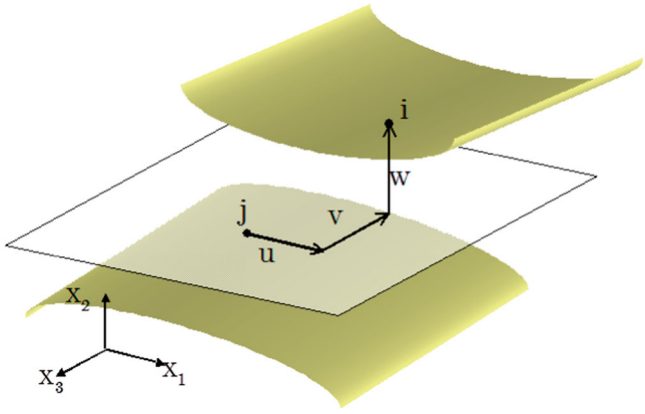

Figure 5. Relative displacement at an interface region.

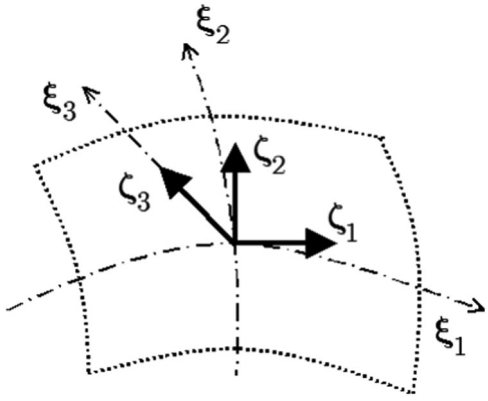

Figure 6. Local Cartesian system.

Within the context of the finite element method, it is these relative displacements that are to be simulated by means of an interface element. Only local behaviour is meant to be simulated by each individual element. The overall behaviour can be simulated by a series of elements placed along the trace of the physical interface (Figure 6).

The element is formulated so as to enable two relative shear displacements and one normal between the top and the bottom faces. Utilising the same mapping for the global displacements as for the coordinates, the global displacements of two originally coinciding points j and i, one on each face of the element, can be expressed in terms of the nodal displacements of the corresponding element face as:

$$\begin{Bmatrix} u_1^i \\ u_2^i \\ u_3^i \\ u_1^j \\ u_2^j \\ u_3^j \end{Bmatrix} = \begin{bmatrix} 0 & \tilde{\mathbf{N}} \\ \tilde{\mathbf{N}} & 0 \end{bmatrix} \begin{Bmatrix} u_{11} \\ u_{12} \\ u_{13} \\ u_{21} \\ : \\ : \\ u_{15\,3} \\ u_{16\,1} \\ u_{16\,2} \\ u_{16\,3} \end{Bmatrix} \tag{6}$$

with

$$\tilde{\mathbf{N}} = \begin{bmatrix} N_1 & 0 & 0 & N_2 & \dots & 0 & N_8 & 0 & 0 \\ 0 & N_1 & 0 & 0 & \dots & 0 & 0 & N_8 & 0 \\ 0 & 0 & N_1 & 0 & \dots & N_7 & 0 & 0 & N_8 \end{bmatrix} \tag{7}$$

or

$$\mathbf{u} = \mathbf{N}\,\tilde{\mathbf{u}} \tag{8}$$

Similarly, the contact stresses $\boldsymbol{\sigma}_c$ between the two contact bodies can be expressed in terms of the nodal contact stresses $\tilde{\boldsymbol{\sigma}}_c$ as:

$$\boldsymbol{\sigma}_c = \mathbf{N}\,\tilde{\boldsymbol{\sigma}}_c \tag{9}$$

2.3. Local Cartesian coordinate system

Three mutually orthogonal axes of material anisotropy are defined. For this reason, at each integration point of the element, a local Cartesian coordinate system ($\zeta_i, \quad i = 1 \dots 3$) is set up as follows:

Axis $\boldsymbol{\zeta}_1$ spans along the vector $\mathbf{v}_{\xi_1}$ tangent to the ξ_1 axis

$$v_{\xi_1} = \left(\frac{\partial X_1}{\partial \xi_1} \quad \frac{\partial X_2}{\partial \xi_1} \quad \frac{\partial X_3}{\partial \xi_1} \right)^T \tag{10}$$

then

$$\boldsymbol{\zeta}_1 = \frac{\mathbf{v}_{\xi_1}}{\|\mathbf{v}_{\xi_1}\|} \tag{11}$$

Axis $\boldsymbol{\zeta}_3$ is defined by the cross product of vector $\mathbf{v}_{\xi_1}$ and vector $\mathbf{v}_{\xi_2}$ tangent to the ξ_2 axis

$$\mathbf{v}_{\xi_2} = \left[\frac{\partial X_1}{\partial \xi_2} \quad \frac{\partial X_2}{\partial \xi_2} \quad \frac{\partial X_3}{\partial \xi_2} \right]^T \tag{12}$$

then

$$\boldsymbol{\zeta}_3 = \frac{\mathbf{v}_{\xi_1} \times \mathbf{v}_{\xi_2}}{\|\mathbf{v}_{\xi_1} \times \mathbf{v}_{\xi_2}\|} \tag{13}$$

Axis $\boldsymbol{\zeta}_2$ is defined by the cross product

$$\boldsymbol{\zeta}_2 = \boldsymbol{\zeta}_3 \times \boldsymbol{\zeta}_1 \tag{14}$$

Here the Cartesian derivatives are defined as:

$$\begin{aligned} \left(\frac{\partial X_i}{\partial \xi}\right)_{\xi=\xi_1,\xi_2} &= \sum_{k=1}^{8} \frac{\partial N_k}{\partial \xi} X_{ki} + \left(\frac{t_k}{2}\right) \xi_3 \sum_{k=1}^{8} \frac{\partial N_k}{\partial \xi} \chi_{ki} \quad i = 1, \dots 3 \\ \left(\frac{\partial X_i}{\partial \xi_3}\right) &= \left(\frac{t_k}{2}\right) \sum_{k=1}^{8} N_k \chi_{ki} \end{aligned} \tag{15}$$

In the above-defined local Cartesian coordinate system, the relative displacements between points j and i can be computed from

$$\begin{Bmatrix} \Delta u_{\zeta_1} \\ \Delta u_{\zeta_2} \\ \Delta u_{\zeta_3} \end{Bmatrix} = \begin{bmatrix} 1 & 0 & 0 & -1 & 0 & 0 \\ 0 & 1 & 0 & 0 & -1 & 0 \\ 0 & 0 & 1 & 0 & 0 & -1 \end{bmatrix} \begin{Bmatrix} u_{\zeta_1}^i \\ u_{\zeta_2}^i \\ u_{\zeta_3}^i \\ u_{\zeta_1}^j \\ u_{\zeta_2}^j \\ u_{\zeta_3}^j \end{Bmatrix} \tag{16}$$

or

$$\Delta \mathbf{u}_\zeta = \mathbf{L}\,\mathbf{u}_\zeta \tag{17}$$

The relation between local interface displacements $\mathbf{u}_\zeta$ and the corresponding global displacements is or

$$\begin{Bmatrix} u^i_{\zeta_1} \\ u^i_{\zeta_2} \\ u^i_{\zeta_3} \\ u^j_{\zeta_1} \\ u^j_{\zeta_2} \\ u^j_{\zeta_3} \end{Bmatrix} = \begin{bmatrix} \cos(\zeta_1, x_1) & \cos(\zeta_1, x_2) & \cos(\zeta_1, x_3) & 0 & 0 & 0 \\ \cos(\zeta_2, x_1) & \cos(\zeta_2, x_2) & \cos(\zeta_2, x_3) & 0 & 0 & 0 \\ \cos(\zeta_3, x_1) & \cos(\zeta_3, x_2) & \cos(\zeta_3, x_3) & 0 & 0 & 0 \\ 0 & 0 & 0 & \cos(\zeta_1, x_1) & \cos(\zeta_1, x_2) & \cos(\zeta_1, x_3) \\ 0 & 0 & 0 & \cos(\zeta_2, x_1) & \cos(\zeta_2, x_2) & \cos(\zeta_2, x_3) \\ 0 & 0 & 0 & \cos(\zeta_3, x_1) & \cos(\zeta_3, x_2) & \cos(\zeta_3, x_3) \end{bmatrix} \begin{Bmatrix} u^i_1 \\ u^i_2 \\ u^i_3 \\ u^j_1 \\ u^j_2 \\ u^j_3 \end{Bmatrix} \tag{18}$$

$$\begin{Bmatrix} u^i_{\zeta_1} \\ u^i_{\zeta_2} \\ u^i_{\zeta_3} \\ u^j_{\zeta_1} \\ u^j_{\zeta_2} \\ u^j_{\zeta_3} \end{Bmatrix} = \begin{bmatrix} \theta & \mathbf{0} \\ \mathbf{0} & \theta \end{bmatrix} \begin{Bmatrix} u^i_1 \\ u^i_2 \\ u^i_3 \\ u^j_1 \\ u^j_2 \\ u^j_3 \end{Bmatrix} \tag{19}$$

or

$$\mathbf{u}_\zeta = \mathbf{T}\,\mathbf{u} \tag{20}$$

Combining Equation (8), Equation (20) and Equation (17) leads to

$$\mathbf{u}_{\text{rel}} = \mathbf{N}\mathbf{L}\,\mathbf{T}\;\tilde{\mathbf{u}} = \mathbf{N}\mathbf{C}\;\tilde{\mathbf{u}} = \mathbf{N}\,\tilde{\mathbf{u}}_{\text{rel}} \tag{21}$$

where $\mathbf{u}_{\text{rel}}$is the local relative displacement vector, $\tilde{\mathbf{u}}_{\text{rel}}$ is its nodal equivalent and $\mathbf{C} = \mathbf{L}\,\mathbf{T}$is a matrix which transforms the global displacement into the local relative displacement. In the next section the constraint equations on the interface to model the non-penetration condition, stick and slip will be discussed.

2.4. Simulation of contact

For simulation of no-penetration, adhesive debonding, stick and frictional slippage between two objects, the interface element described in the previous section has the capability to undergo certain constraint conditions.

2.4.1. Virtual work

The contact virtual work for a contact interface element is defined as

$$\delta\mathbf{u}^{\mathbf{T}}\,\mathbf{F}_c = \int (\delta\mathbf{u}^{\mathbf{T}}_{\mathbf{rel}}\,\boldsymbol{\sigma}_c)\,\mathrm{d}\Gamma \tag{22}$$

where $\delta\mathbf{u}$ is the virtual displacement vector, $\delta\tilde{\mathbf{u}}_{\mathbf{rel}}$ is the virtual relative displacement vector, $\mathbf{F_c}$ is the contact force vector, $\tilde{\boldsymbol{\sigma}}_{\mathbf{c}}$is the contact stress vector and Γ is the surface area of the contact interface. All quantities are continuous field variables. The variables $\delta\mathbf{u}$ and $\mathbf{F_c}$are defined in the global Cartesian coordinate system, while $\delta\mathbf{u}_{\mathbf{rel}}$ and $\boldsymbol{\sigma}_{\mathbf{c}}$ are defined in the local Cartesian coordinate system of the interface element.

With the help of Equations (9) and 21, the virtual work in Equation (22) can be rewritten into its nodal equivalent as:

$$\begin{aligned}
\delta\mathbf{u}^T\,\mathbf{F}_c &= \int_\Gamma \delta\mathbf{u}^T_{rel}\,\boldsymbol{\sigma}_c\,d\Gamma = \int_\Gamma (\mathbf{N}\,\delta\tilde{\mathbf{u}}_{rel})^T\,\mathbf{N}\,\tilde{\boldsymbol{\sigma}}_c\,d\Gamma = \\
&= \int_\Gamma ((\mathbf{N}(\mathbf{L}\,\mathbf{T}\,\delta\tilde{\mathbf{u}}))^T\mathbf{N}\tilde{\boldsymbol{\sigma}}_c)\,d\Gamma = \int_\Gamma ((\mathbf{N}(\mathbf{C}\,\delta\tilde{\mathbf{u}}))^T\mathbf{N}\tilde{\boldsymbol{\sigma}}_c)\,d\Gamma = \\
&= \int_\Gamma (\mathbf{C}\,\delta\tilde{\mathbf{u}})^T\mathbf{N}^T\mathbf{N}\,\tilde{\boldsymbol{\sigma}}_c\,d\Gamma = \int_\Gamma \delta\tilde{\mathbf{u}}^T\mathbf{C}^T(\mathbf{N}^T\mathbf{N})\,\tilde{\boldsymbol{\sigma}}_c\,d\Gamma = \\
&= \int_\Gamma \delta\tilde{\mathbf{u}}^T\mathbf{C}^T\mathbf{S}\,\tilde{\boldsymbol{\sigma}}_c\,d\Gamma = \int_\Gamma \delta\tilde{\mathbf{u}}^T\,\tilde{\mathbf{F}}_c\,d\Gamma
\end{aligned} \tag{23}$$

where $\mathbf{S} = \int \mathbf{N}^T\mathbf{N}\,d\Gamma$ is the surface area matrix.

From Equation (23) it can be derived that the nodal contact forces for node pair i in the global Cartesian coordinate system $\tilde{\mathbf{F}}_c$ are defined as:

$$\tilde{\mathbf{F}}_c = \mathbf{C}^T\mathbf{S}\,\tilde{\boldsymbol{\sigma}}_c = \mathbf{C}^T\,\bar{\mathbf{F}}_c \tag{24}$$

where $\bar{\mathbf{F}}_c = \mathbf{S}\,\tilde{\boldsymbol{\sigma}}_c$is the contact force in the local axis system of the contact element.

2.4.2. Constraint equations

This section describes the constraint equations to model the non-penetration condition, stick and frictional slippage between two objects.

For every node pair a set of constraint equations can be build, which has the following form:

$$\mathbf{R}\cdot\mathbf{C}\cdot\tilde{\mathbf{u}} + (\mathbf{I}-\mathbf{R})\tilde{\boldsymbol{\sigma}}_c = \mathbf{R}\,\mathbf{a} + (\mathbf{I}-\mathbf{R})\,\mathbf{b} \tag{25}$$

Here $\mathbf{R}$ is the contact state matrix, which is explained later, $\mathbf{I}$ is the identity matrix, $\tilde{\boldsymbol{\sigma}}_c$ is the nodal contact stresses, $\mathbf{a}$ is the prescribed relative displacements and $\mathbf{b}$ is the prescribed contact stresses, and $\mathbf{C}$ has been defined in Equation (21).

Furthermore, the constraint equation in Equation (25) can be recast in the more compact form as:

$$\mathbf{h} = \begin{bmatrix} \mathbf{R}\,\mathbf{C} & \mathbf{I}-\mathbf{R} \end{bmatrix} \begin{bmatrix} \tilde{\mathbf{u}} \\ \tilde{\boldsymbol{\sigma}}_c \end{bmatrix} - \mathbf{a}^* = \mathbf{0} \tag{26}$$

where

$$\mathbf{a}^* = \mathbf{R}\,\mathbf{a} + (\mathbf{I}-\mathbf{R})\,\mathbf{b}$$

Table 1. Definition of the R matrix per contact state.

Contact state	R(1,1) (ζ_1 axis)	R(2,2) (ζ_2 axis)	R(3,3) (ζ_3 axis)
Stick	1	1	1
Free	0	0	0
Slip	0	0	1

The contact state matrix $\mathbf{R}$ is a 3×3 diagonal matrix with zeros and ones indicating one of the three states: free, stick and slip, Table 1. For the adhesive contact element presented in this thesis, the stick state is not used and thus not activated.

It can be seen, that depending on the R-values, the corresponding values on the right-hand side of Equation (25) are either a prescribed relative displacement (value 1) or a prescribed contact stress (value 0). The magnitude of these prescribed relative displacements or contact stresses depends on the state transition. For example, if a node pair is in a free state and overlap occurs, the state is set to stick so that a relative displacement correction can be applied in the next iteration to prevent this overlap. More details about state transitions with their corresponding prescribed relative displacements or contact stresses can be found in Swoboda and Lei (1994).

The schematics in Figure 7 present the three main contact states defined by the contact algorithm, as well as the local coordinate orientation. For the sake of clarification, in the figure, the contact states are depicted by faces and bodies, though in reality the state is evaluated on the terms of node-pairs, see Figure 2.

2.4.3. Incremental solution of global system of equations

To satisfy equilibrium the following coupled optimisation problem has to be solved:

$$\begin{aligned}&\text{minimize function } \mathbf{g}, \text{ where } \mathbf{g} = \mathbf{K}\cdot\tilde{\mathbf{u}} + \mathbf{C}^{\mathrm{T}}\cdot\mathbf{S}\cdot\tilde{\boldsymbol{\sigma}}_c - \mathbf{F}\\ &\text{minimize function } \mathbf{h}, \text{ where } \mathbf{h} = \mathbf{R}\cdot\mathbf{C}\cdot\tilde{\mathbf{u}} + (\mathbf{I}-\mathbf{R})\cdot\tilde{\boldsymbol{\sigma}}_c - \mathbf{a}^*\end{aligned} \tag{27}$$

in which $\mathbf{g}$ is the residual force function and $\mathbf{h}$ is the contact constraint function defined in Equation (26). Furthermore, $\mathbf{K}$ is the global stiffness, $\mathbf{S}$ is defined in Equation (23), $\mathbf{F}$ is the externally applied load, $\mathbf{R}$is the contact state matrix, $\mathbf{a}^*$ is the contact constraint vector, and $\mathbf{C}$ has been defined in Equation (21).

For the solution of the optimisation problem a Newton–Raphson iteration scheme can be defined:

$$\begin{aligned}&\begin{bmatrix}\partial\mathbf{g}/\partial\tilde{\mathbf{u}} & \partial\mathbf{g}/\partial\tilde{\boldsymbol{\sigma}}_c\end{bmatrix}\begin{bmatrix}\Delta\tilde{\mathbf{u}}\\ \Delta\tilde{\boldsymbol{\sigma}}_c\end{bmatrix} = -\mathbf{g} \text{ with } \partial\mathbf{g}/\partial\tilde{\mathbf{u}} = K \text{ and } \partial\mathbf{g}/\partial\tilde{\boldsymbol{\sigma}}_c = \mathbf{C}^{\mathrm{T}}\mathbf{S}\\ &\begin{bmatrix}\partial\mathbf{h}/\partial\tilde{\mathbf{u}} & \partial\mathbf{h}/\partial\tilde{\boldsymbol{\sigma}}_c\end{bmatrix}\begin{bmatrix}\Delta\tilde{\mathbf{u}}\\ \Delta\tilde{\boldsymbol{\sigma}}_c\end{bmatrix} = -\mathbf{h} \text{ with } \partial\mathbf{h}/\partial\tilde{\mathbf{u}} = R\cdot\mathbf{C} \text{and} \partial\mathbf{h}/\partial\tilde{\boldsymbol{\sigma}}_c = \mathbf{I}-\mathbf{R}\end{aligned} \tag{28}$$

or

$$\begin{bmatrix}\mathbf{K} & \mathbf{C}^{\mathrm{T}}\mathbf{S}\\ \mathbf{RC} & \mathbf{I}-\mathbf{R}\end{bmatrix}\times\begin{bmatrix}\Delta\tilde{\mathbf{u}}\\ \Delta\tilde{\boldsymbol{\sigma}}_c\end{bmatrix} = \begin{bmatrix}\mathbf{F} - {}^{t-\Delta t}\mathbf{F}_{\mathbf{int}} - \mathbf{C}^{\mathrm{T}}\mathbf{S}\,{}^{t-\Delta t}\tilde{\boldsymbol{\sigma}}_c\\ \Delta\mathbf{a}^*\end{bmatrix} \tag{29}$$

Here the term $\mathbf{F}_{\mathbf{int}} = \mathbf{K}\,\tilde{\mathbf{u}}$ is the sum of the internal loads of all the elements except the contact interfaces in the previous converged step/iteration. For the contact interface elements, internal loads are represented by the term $\mathbf{C}^{\mathrm{T}}\,\mathbf{S}\,{}^{t-\Delta t}\tilde{\boldsymbol{\sigma}}_c$.

In the system of equations as defined in Equation (29) not only the values of the displacements and the contact stresses are changing during iterations but, also, the contact states.

For every global iteration, the contact state is determined, which means that for every contact node pair, new values for the contact state matrix $\mathbf{R}$ and incremental contact constraint vector $\Delta\,\mathbf{a}^*$ are set. The system of equations in Equation (29) is then solved for the increments of displacement and contact stress. Those increments are used to retrieve updated values of contact stresses and displacements.

It should be noted that the contact interface elements are constraint elements, which do not have stiffness and therefore do not contribute to the global stiffness $\mathbf{K}$ in Equation (29). In the case that all three constraints of all contact node pairs of a contact interface are stress controlled, i.e. $\mathbf{R}$=$\mathbf{0}$, the contact element stiffness matrix becomes:

$$\mathbf{K}_{el} = \begin{bmatrix}\mathbf{0} & \mathbf{C}^{\mathrm{T}}\mathbf{S}\\ \mathbf{0} & \mathbf{I}\end{bmatrix} \tag{30}$$

This matrix is clearly singular. The consequence hereof is that the global stiffness matrix is consisting of two or more independent parts, for which each part has to be constrained such that it is statically determined. Therefore, in this study, the contact interfaces are enhanced with a pseudo stiffness. This will prevent the singularity of the global stiffness matrix, at

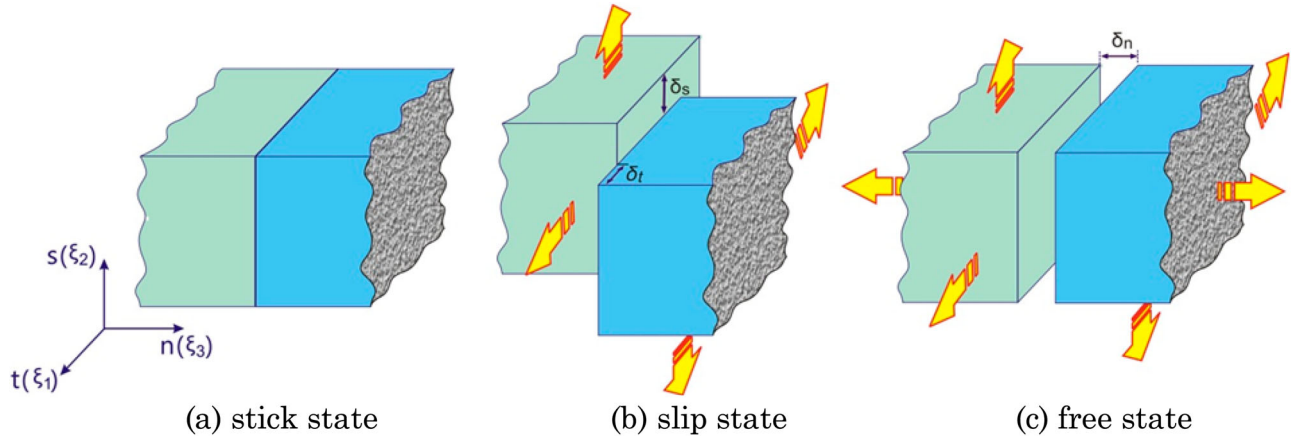

Figure 7. Schematic of the three main contact states. (a) stick state, (b) slip state, (c) free state.

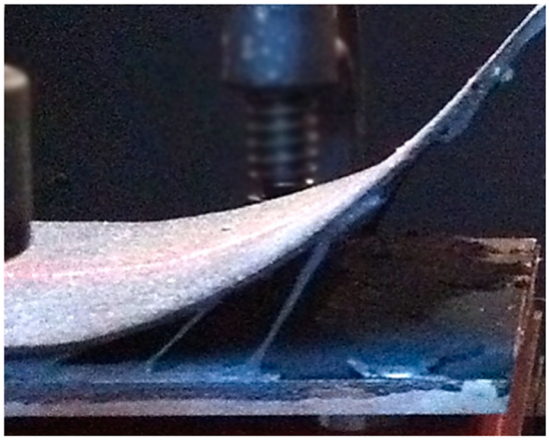

Figure 8. A debonding membrane of a MAT test [2].

the expense of generating non-real internal forces. Those forces are cancelled by adding counter acting external forces on the right-hand side of Equation (29) at equilibrium, see Appendix A.

2.5. Simulation of adhesion

Interfacial fibrillation is a typical mechanism that frequently occurs during debonding of membranes from substrates, Figure 8. It involves large displacements at the interface as well as large deformations in the membrane material.

Under large displacements, it is no longer physical to discriminate between normal and tangential openings. In the case of membrane debonding from substrates, such large displacements are bridged by fibrils, which act more or less like non-linear springs and transfer load only along their axis. Therefore, a generic adhesive zone constitutive model is introduced that describes the process of membrane debonding on the basis of fibrillation, Figure 9. The adhesive traction-separation law prevents the contact interface to freely separate as soon as it undergoes tensile forces.

The adhesive zone constitutive model which is utilised to describe the traction-separation relation of fibrillation is controlled by a constitutive relation between traction force and the opening displacement along the fibril axis. Based on the work of van den Bosch and Schreurs (2008), the adhesive traction-separation law is defined as:

$$\mathrm{T} = \frac{G}{\delta_C}\left(\frac{\Delta}{\delta_C}\right)\exp\left(-\frac{\Delta}{\delta_C}\right) \tag{31}$$

where G as shown in Figure 9, is the strain energy release rate that is characterised as the energy per unit crack length required for crack/debonding extension, δ_C is the characteristic opening length of the fibril, Δ is the relative displacement of a node pair which constitutes the fundamental physical quantity controlling the magnitude of the debonding stress. If $\Delta \geq \delta_C$, the traction force along the fibril starts to decrease. The peak traction value equals

$$\mathrm{T}_{\max} = \frac{G}{\delta_C \exp(1)} \tag{32}$$

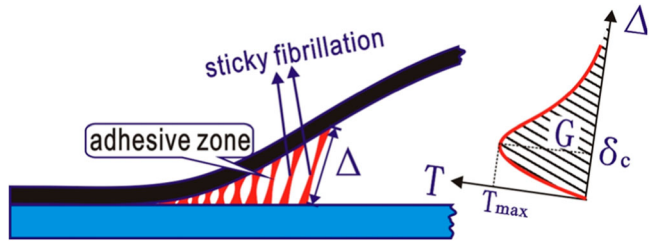

Figure 9. Schematic of traction separation at interface.

Upon unloading, if the traction force has not reached the peak value $\mathrm{T}_{\max}$, the adhesive zone law follows a reversible response indicated as (i) in Figure 10 back to the origin, i.e. no degradation accumulates at the interface. If the traction force has already passed the peak value, a linear elastic unloading behaviour indicated as (ii) in Figure 10 is shown.

To give a conceptual representation of the traction-separation law, two sets of the relation are plotted: (1) δ_C=2.0 mm, G=1.0, 2.0 and 3.0 N/mm, Figure 11; (2) G=4.0 N/mm, δ_C=1.0, 1.5 and 2.0 mm, Figure 12.

The accuracy of utilising Equation (31) for simulating the process of membrane debonding from a substrate will be examined in the model verification part of this paper.

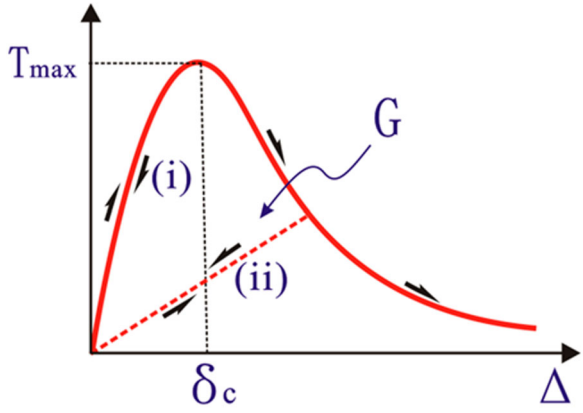

Figure 10. Schematic traction-separation relation.

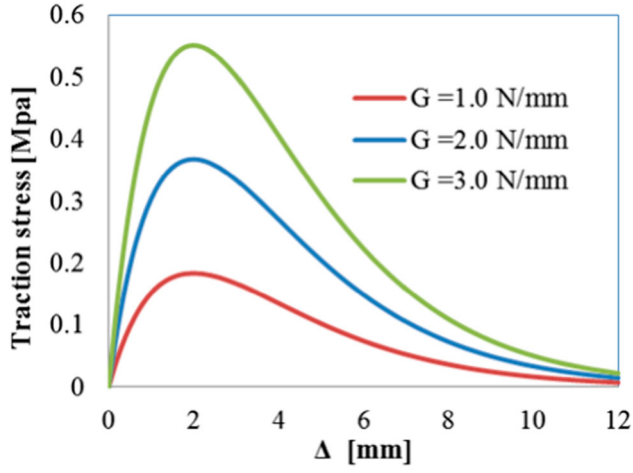

Figure 11. Response curves at different G values (δ_C=2.0 mm).

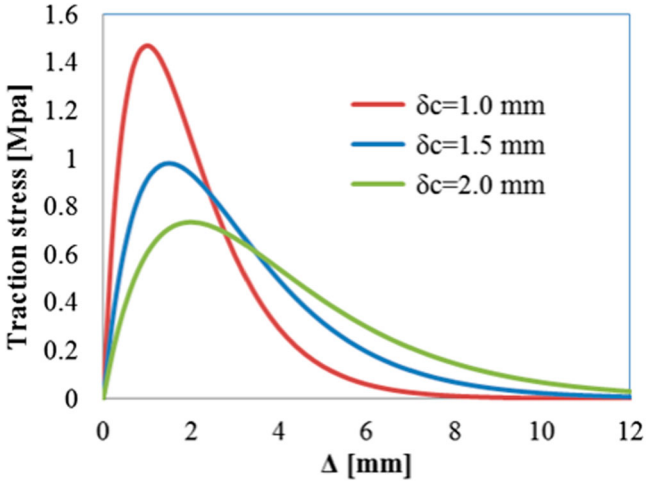

Figure 12. Response curves at different δ_C values (G=4.0 N/mm).

To incorporate this traction-separation law into the numerical algorithm in 2.4.3 the active contact states with their corresponding contact stress/relative displacement corrections $\mathbf{\Delta}\ \mathbf{a}^*$ have to be determined.

Three contact states are involved in the algorithm of the adhesive contact finite element, Figure 13. Body A and B are a pair of contact objects, for illustration purpose here, only body B is moving and body A is stationary, with a node pair located between these two bodies. The original normal distance of this node pair is denoted as D before any relative normal displacement Δuhappens. If the two bodies are separating, $\Delta u > 0$; if these two bodies are moving closer to each other, $\Delta u < 0$. Three contact states can be distinguished based on D andΔu values:

(1) Debonding ($\Delta u > 0$). In this case, the faces of the contact interface are separating (i.e. the relative normal displacement of the faces/node pairs is positive). This separation is controlled by the traction-separation law presented previously.
(2) Contact-free ($-D \leq \Delta u \leq 0$). This state occurs when the faces of the contact interface can move freely with respect to each other in the range of distance from 0 to D, but in such a way that, a non-overlapping condition is created.
(3) Attaching/sliding ($-D > \Delta u$), this is a slip state. The faces of the contact interface have to be prevented from overlapping along the interface normal direction. In the tangential directions, i.e. in plane, the interface is allowed to displace.

For these three contact states the following contact resisting stress / relative displacement corrections are enforced:

- Debonding: in all three local interface directions the adhesive law is used to correct the contact stress $\tilde{\sigma}_c$, i.e. $(\Delta a^*)_{1..3} = (T - \sigma_{el} - \tilde{\sigma}_c)_{1..3}$. T is the stress defined by the traction-separation law, σ_{el} is the pseudo elastic stress of the contact interface and $\tilde{\sigma}_c$ is the already present contact stress.
- Contact-free: in normal as well as tangential interface directions the contact stresses due to the introduced contact element stiffness are released, i.e. $(\Delta a^*)_{1..3} = -(\sigma_{el})_{1..3}$.
- Attaching/sliding: the amount of overlap in the interface normal direction has to be corrected, i.e. $(\Delta a^*)_3 = -(\Delta u_r)_3$. Here $(\Delta u_r)_3$ is the amount of overlap. In the tangential interface directions the traction-separation law is applied. The stress correction in these directions is defined to be $(\Delta a^*)_{1,2} = (T - \tilde{\sigma}_c)_{1,2}$.

The detail explanations of the contact resisting stress/relative displacement corrections can be found in Appendix A. The abovementioned contact states address all three basic cracking modes of fracture mechanics: opening (normal), shearing and tearing (tangential) modes, Figure 14. The 'debonding' state could be referred to the opening as well as mixing modes of both normal and tangential components. The 'attaching/sliding' state is comparable to the shearing and tearing modes. The validity of the present adhesive contact element is demonstrated in the following section.

2.6. Model verification

In order to examine the adhesive contact interface element with the traction-separation material law, model verifications are done by comparing the results of numerical simulations, analytical solutions and experimental measurements. These simulations include: (1) a strip footing problem to verify the contact behaviour of the element; (2) a double cantilever beam problem, aiming to test the pure opening state of the element; (3) a shear box simulation to test the sliding and debonding behaviour of the element.

2.6.1. Strip footing problem

In this section, the interface contact behaviour has been verified by using a strip footing problem. This problem has been approached theoretically by several researchers. Herein, the

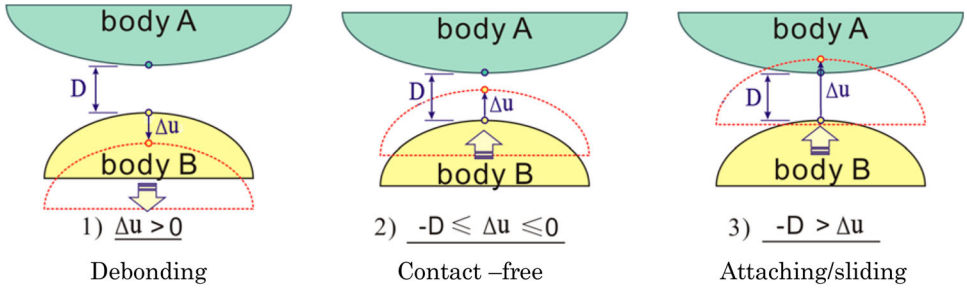

Figure 13. Three contact states of adhesive contact finite element

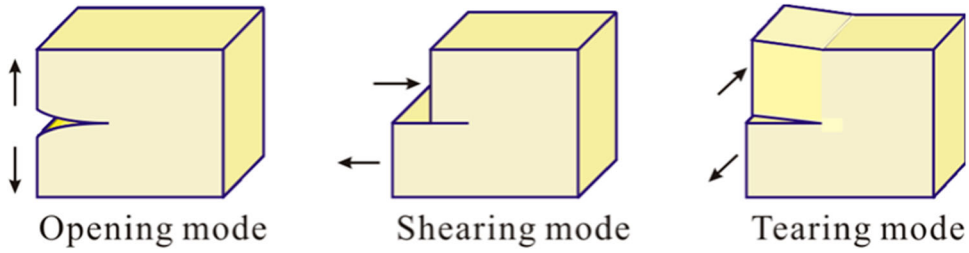

Figure 14. Three basic cracking modes.

setup of Lei *et al.* (1995) is replicated. For this analysis, the finite element mesh is composed of a loading block and a footing block. The mesh and material parameters of the blocks are given in Figure 15. Cohesionless and frictionless contact conditions are assumed between the loading block and the footing block. The input parameters for the contact interface are G=0.001 N/mm, δ_c=0.1 m. E=2×10^3 N/mm^2, and ν=0.3 are utilised for modelling the blocks.

The loading block is initially suspended above the footing block, with an initial contact element thickness of 1 mm. The bottom boundary of the footing block is fixed and all the other boundaries around the footing block are free to move. The loading procedure is applied via displacement control on the upper surface of the loading block, Figure 16. As time increase, the loading block is firstly lowered toward the footing and later lifted upwards.

The numerical results show that the contact element effectively prohibits overlapping and creates realistic contact, slippage and separation between two adjacent bodies. The block deformation during the loading process can be seen in Figure 17.

Figure 18 demonstrates the comparison between theoretically and numerically computed normal contact stresses along the edge of the footing. The theoretical solution for this problem shows a stress concentration near the edge of the footing. The results show a good agreement between the two analyses.

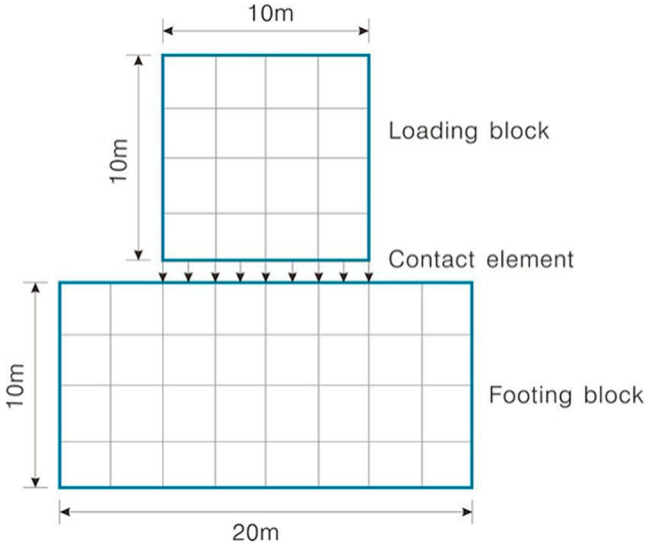

Figure 15. Dimension of strip footing load model.

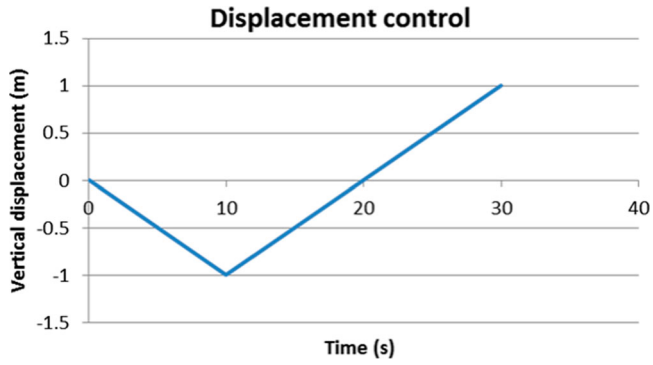

Figure 16. The loading scheme.

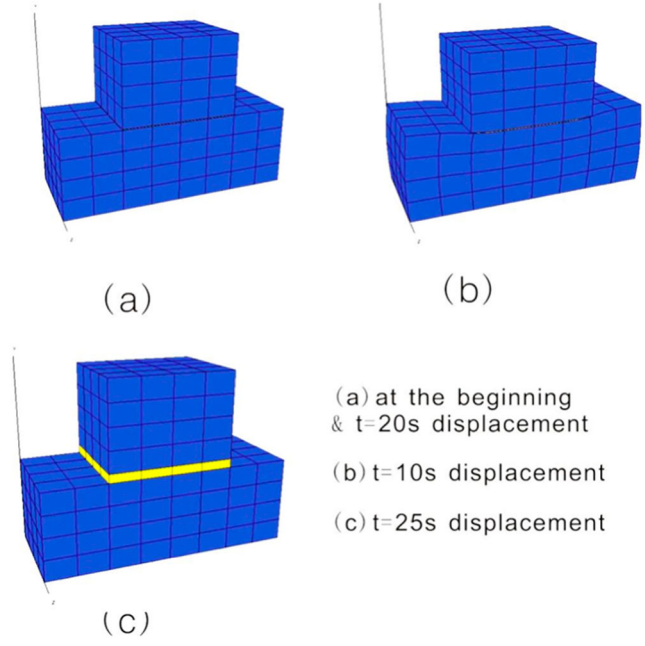

Figure 17. The deformation configuration during the loading process.

2.6.2. Numerical simulation of double cantilever beam problem

A double cantilever beam (DCB) specimen is used to study crack opening and growth. This simulation aims at testing the debonding state of the adhesive contact element. The configuration and the FE mesh are illustrated in Figure 19. The dimensions of the specimen are 150×25×4 mm. The length of an initial crack notch is 30 mm. An adhesive contact layer of 100 mm is located in front of the initial crack notch. The

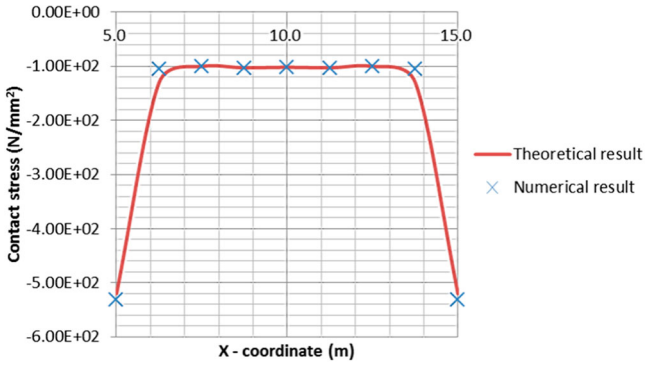

Figure 18. Normal contact stresses along the footing.

analysis is performed by applying a displacement-controlled load at the left end of the upper beam surface.

The following properties have been chosen in order to replicate the experimental work by Robinson & Song (1992) for comparison. For the beam material, the material parameters utilised for this numerical example are:

E=126000 MPa, $\nu = 0.263$

and for the adhesive contact interface element, the following model parameters are used:

G=0.281 N/mm, δ_C=0.5 mm

The crack development at the last loading step is shown in Figure 20. The distributions of horizontal and normal stresses in the beam are shown in Figure 21 and Figure 22 respectively.

Both the capability and the accuracy of the adhesive contact interface element with the traction-separation material law can be examined by comparing the numerical predictions of the beam response with the observed laboratory behaviour.

Figure 23 presents the comparison of the numerical predictions with the experimental result in term of the load and deflection at the beam tip. The model parameters utilised for such comparison are determined on the basis of the basic material tests.

It can be seen that the overall load/deflection solution obtained by the finite element simulation shows good agreement with the experimental result. The load fluctuations of the numerical results can be smoothened by utilising a finer mesh. It can be concluded that the adhesive contact interface element with the traction-separation material law is appropriate for description of the actual material layer debonding behaviour.

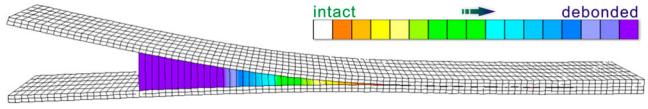

Figure 20. Crack propagation and mesh deformation.

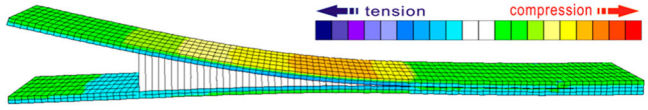

Figure 21. Distribution of horizontal stress.

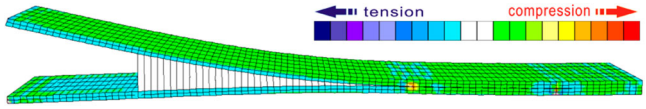

Figure 22. Distribution of normal stress.

2.7. Simulation of fatigue damage accumulation

Cyclic loading, in the multilayer surfacing system on orthotropic steel deck bridges, lead to material fatigue damage. Accumulation of these micro degradations can initiate debonding at the interfaces in the multilayer surfacing system. Laboratory cyclic tests on fatigue resistance of surfacing systems on orthotropic steel allow to predict and to take into account material fatigue performances in OSDB pavement design.

In the past, various laboratory fatigue tests for modelling asphalt concrete surfacing material have been proposed as well as different interpretation methods. Differences between results of one type of test to another show the difficulties in determining the intrinsic characteristics of the asphalt mixes fatigue damage processes.

The fatigue life assessment of membrane bonded on OSDB has not yet been sufficiently investigated. Inspection results of OSDB have shown that the working life of asphalt surfacings

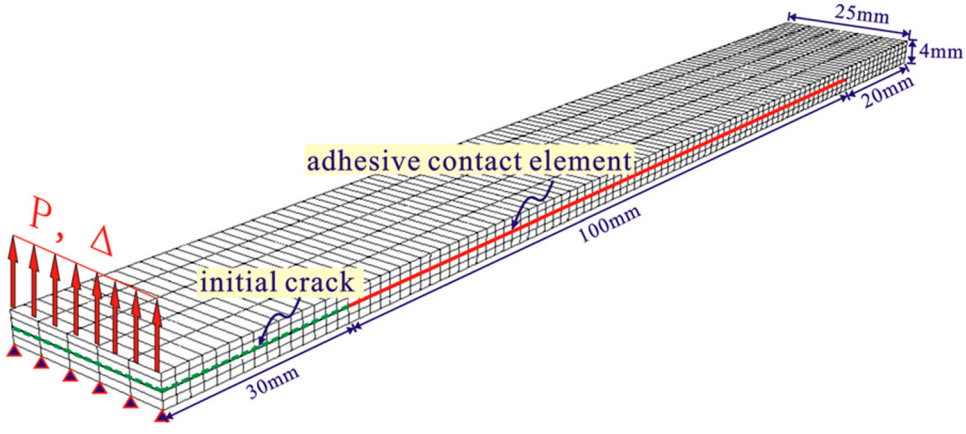

Figure 19. FE mesh of double cantilever beam.

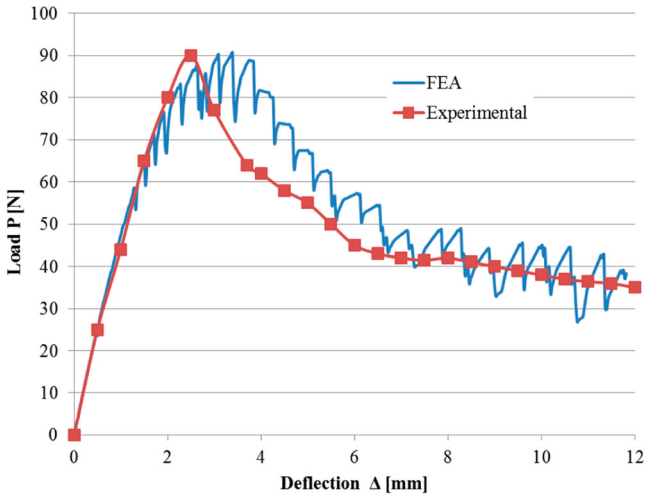

Figure 23. Load/deflection relationship for double cantilever beam.

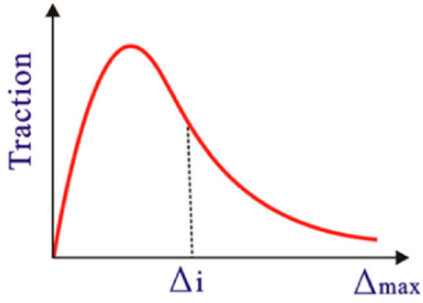

Figure 24. Damage index for adhesive contact element.

is influenced significantly by the fatigue damage in the membrane bonding layers. This means that particular attention must be paid on studying the fatigue response at the bonding interfaces in multilayer surfacing system.

In this study, by modifying the adhesive traction-separation law in Equation (31), a methodology for modelling fatigue damage accumulation at the adhesive contact interface element is proposed. A damage parameter D_i is defined which can vary from 0 (no damage) to 1 (complete damage), and which is related to the bonding strength degradation at the contact interface. The damage parameter D_i is a scalar quantity, which can be specified by the following formulation:

$$D_i = \frac{\Delta_i}{\Delta_{\max}} \tag{33}$$

where Δ_i is the instantaneous fibril displacement along the fibril axis of the interface subjected to load P, $\Delta_{\max}$ is the maximum displacement associated with complete bond strength degradation, Figure 24.

In this study, for a cyclic test, a quantity related to the fibril deformation Δ_i is introduced into the proposed fatigue damage model. The relation between the inelastic deformation related quantity ξ and the fibril deformation Δ_i can be expressed:

$$\xi = \xi_{\min}(M^c - 1) \tag{34}$$

in which $\xi_{\min}$ and c are a material parameter. M is the number of load cycle. Figure 25 shows the variation of ξ versus the

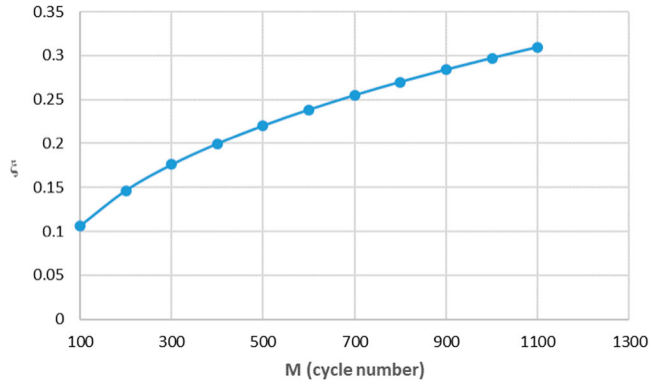

Figure 25. ξ versus the load cycle M (ξ_{min}=0.2, c=0.4).

number of load cycle M. ξ increases as the number of load cycle develops.

The characteristic opening length δ_C in Equation (31) is defined based on the inelastic deformation related quantity ξ:

$$\delta_c = \delta_{\max} + (\delta_0 - \delta_{\max})e^{-k_1\xi} \tag{35}$$

where δ_0 is the initial characteristic opening length of the interface, $\delta_{\max}$is the ultimate characteristic opening length. k_1 is a parameter that controls the changing rate of δ_c.

By substituting the inelastic strain trajectory ξin Equation (34) into Equation (35), the variation of δ_C versus ξ can be obtained. Figure 26 shows an example curve of δ_C with the parameter ξ when c=0.4, k_1=0.6, δ_0=1 mm and $\delta_{\max}$ = 5mm. It can be observed that the characteristic debonding length δ_C increases as the number of load cycle increases (ξ increases with the increasing load cycle numbers, see Figure 25).

Figure 27 illustrates the principle of this cumulative damage approach. According to Equation (33), the peak traction force T_{max} represents the bonding strength of the contact adhesive interface together with δ_C governing the shape of the traction-separation function. The strain energy release rate G in Equation (31) is a basic physical quantity of the adhesive interface element, which is regarded to be constant. Once the characteristic debonding length δ_C is increased, the resultant peak traction force (bonding strength of the contact adhesive interface) in the model will be decreased, hence, the model

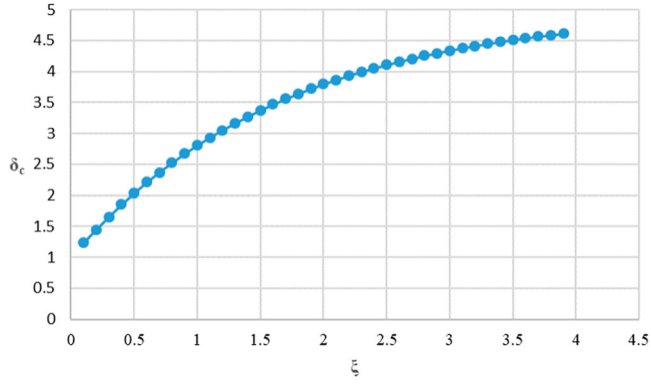

Figure 26. δ_C as a function of ξ.

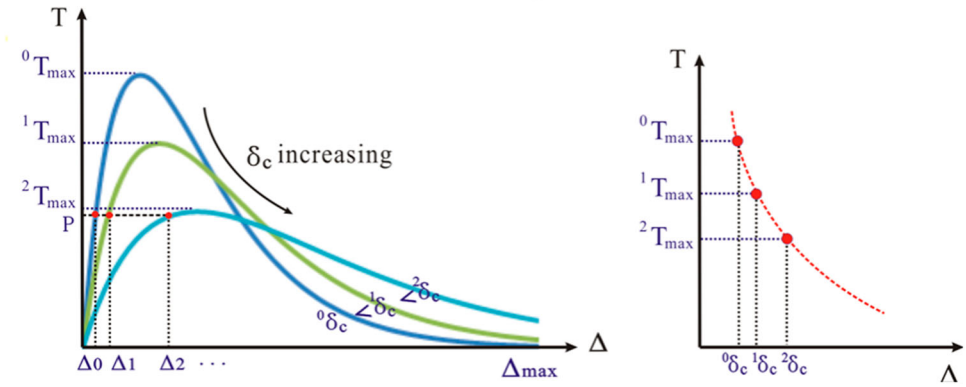

Figure 27. Concept of accumulative damage approach.

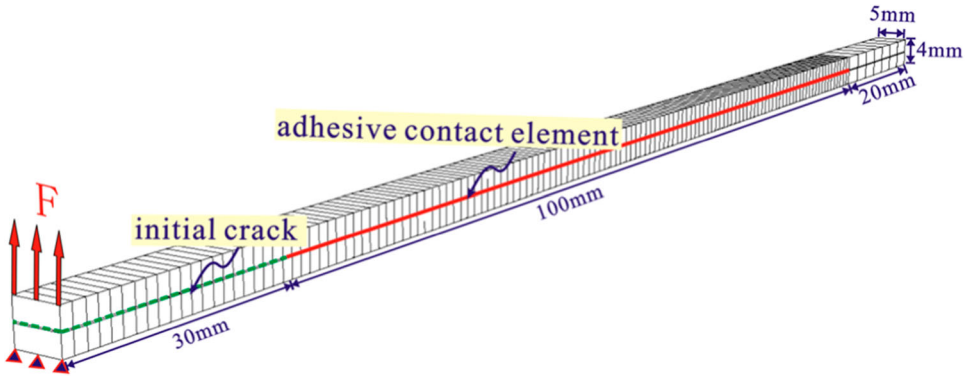

Figure 28. FE mesh of double cantilever beam.

curve tends to be flatter. At a constant cyclic load P, due to the reduction of the peak traction force, the fibril displacement Δ_i along the fibril axis of the interface will increase. Therefore, by applying the fatigue damage definition in Equation (33), the fatigue strength degradation at the adhesive contact interface element can be simulated.

The in-time development of damage at the interfacial zone of a double cantilever beam simulation is shown in Figure 28. The geometry of the beam is similar to the numerical example utilised in Section 2.6.2. An adhesive contact interface element layer of 100 mm is created after the 30 mm initial crack notch, Figure 28. A cyclic load at a frequency of 5 Hz with amplitude F=10 N is applied to the left end of the upper beam surface, Figure 29.

The model parameters utilised for this numerical example are: G=4.0 N/mm, $\delta_C = 1.5$mm, $\Delta_{max} = 8$ mm, c=0.4, $\xi_0 = 1.0$, k_1=30, $\delta_0 = 1$mm and $\delta_{\max} = 5$mm.

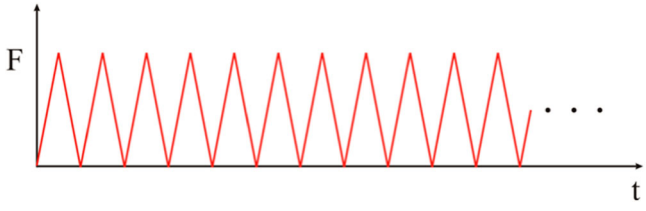

Figure 29. Applied shear load to the shear-box mesh.

Figure 30 shows the accumulated damage at the adhesive contact interface layer within 35000 load cycles. The damage value starts from 0 to 1, representing the states of no-debonding and fully debonded, respectively. It can be observed that, during the first 25,000 load cycles, the development of damage at the interface layer shows steady response. After the 25,000 load cycles, the damage at the interface layer is developed quickly until fracture of the entire specimen.

Figure 31 shows contour plots of accumulative damage (delamination) at the adhesive contact interface layer at number of loading cycles: 1000, 10,000, 30,000 and 35,000

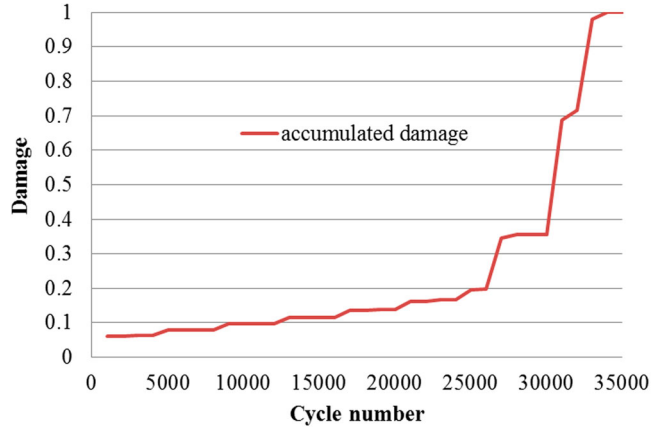

Figure 30. Damage development at the adhesive contact interface.

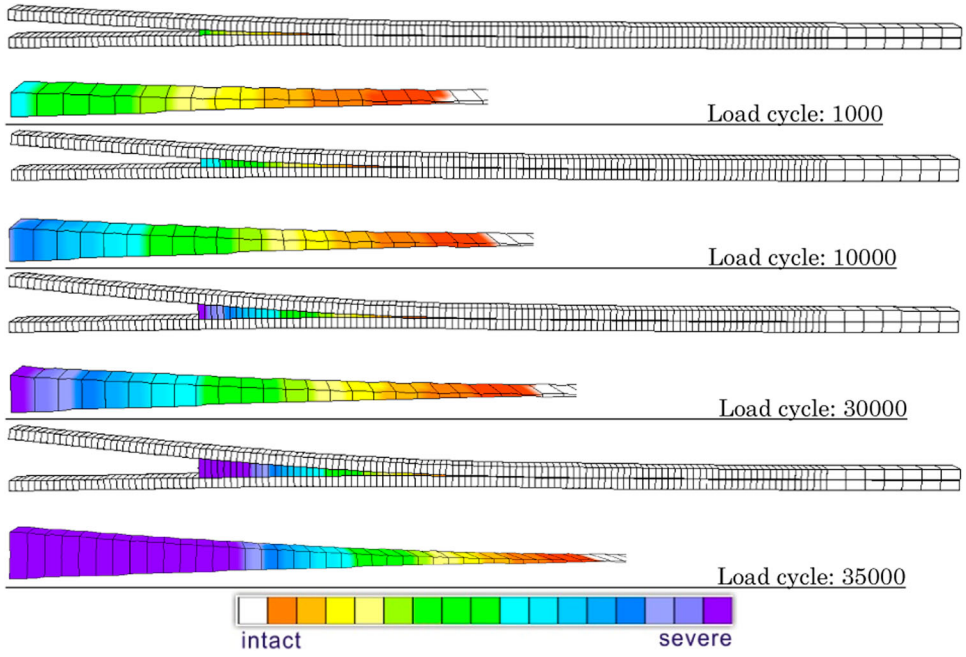

Figure 31. Contour plots of accumulative damage and crack propagation.

respectively. It is shown that delamination in the adhesive contact layer takes place through a process of fatigue damage development. This mechanism involves large displacements and deformations both at the interfacial zone and in the surrounding bulk materials.

3. Conclusions

In this contribution, the following main findings and remarks can be drawn:

- The adhesive traction-separation law that is utilised for the contact interface element in the FE simulation is capable to model the debonding process of a layer material from a substrate.
- by controlling the variation of the characteristic length parameter, the adhesive traction-separation model can provide consistent and satisfactory modelling of the adhesive contact interfacial zone.
- Availability of the constitutive model will allow in the future a better understanding of damage development at the interfacial zone between layers, allowing thus optimisation of their design.
- Further study should be done on the development of experimental methods that are able to determine the associated model parameters. Non-isothermal effects should be introduced into the model parameters to model the heat effects on the fatigue response of the adhesive contact interface layer.

Acknowledgements

This work is part of the research programmme of InfraQuest. InfraQuest is a collaboration between Rijkswaterstaat, TNO and the Delft University of Technology. This research project is funded by the Dutch Ministry of Transport, Public Works and Water Management (RWS). Their financial support is highly appreciated.

Disclosure statement

No potential conflict of interest was reported by the author(s).

References

Chandra, N., *et al.*, 2002. Some issues in the application of cohesive zone models for metal–ceramic interfaces. *International Journal of Solids and Structures*, 39, 2827–2855.

De Borst, R, 2003. Numerical aspects of cohesive-zone models. *Engineering Fracture Mechanics*, 70, 1743–1757.

Lei, X.Y., Swoboda, G., and Zenz, G, 1995. Application of contact-friction interface element to tunnel excavation in faulted rock. *Computers and Geotechnics*, 17, 349–370.

Li, J., 2015. *Optimum design of multilayer asphalt surfacing systems for orthotropic steel deck bridges*. Thesis (PhD). the Netherlands: Delft University of Technology.

Liu, X. (2003). *Numerical modelling of porous media response under static and dynamic load conditions.* Thesis (PhD). the Netherlands: Delft University of Technology.

Liu, X., *et al.*, 2004. Numerical modelling of nonlinear response of soil, part 1: constitutive model. *International Journal of Solids and Structures*, 42 (7), 1849–1881.

Liu, X., *et al.*, 2008. Experimental and numerical characterization of a membrane material for orthotropic steel deck bridges: part 2-development and implementation of a nonlinear constitutive model. *Finite Elements in Analysis and Design*, 44, 580–594.

Liu, X., *et al.*, 2010. Characterisation of surfacing materials for orthotropic steel deck bridges, part 2: numerical work. *International Journal of Pavement Engineering*, 11 (3), 255–265.

Liu, X., *et al.*, 2013. Test method to assess bonding characteristics of membrane layers in wearing course on orthotropic steel bridge decks. *Transportation Research Record*, 2360, 77–83.

Medani, T. O., *et al.*, 2008. Experimental and numerical characterization of a membrane material for orthotropic steel deck bridges: part 1 experimental work and data interpretation. *Finite Elements in Analysis and Design*, 44, 552–563.

Medani, T. O., *et al*., 2010. Characterisation of surfacing materials for orthotropic steel deck bridges - part 1: experiment work. *International Journal of Pavement Engineering*, 11 (3), 237–253.
Robinson, P. and Song, D.Q., 1992. A modified DCB specimen for Mode I testing of multidirectionall Laminates. *Journal of Composite Materials*, 26 (11), 1554–1577.
Scarpas, A. 1992. *CAPA-3D finite elements system user's manual, parts I, II and III.* Delft: Department of Structural Mechanics, Faculty of Civil Engineering, Delft University of Technology.
Swoboda, G. and Lei, X.Y., 1994. Simulation of arch dam foundation interaction with a new friction interface element. *International Journal for Numerical and Analytical Methods in Geomechanics*, 18 (9), 601–617.
Tvergaard, V, 1990. Effect of fibre debonding in a whiskerreinforced metal. *Materials Science and Engineering: A*, 125, 203–213.
Tzimiris, G. 2017. *Experimental investigation of membrane materials used in multilayer surfacing systems for orthotropic steel deck bridges*. Thesis (PhD). Delft University of Technology, the Netherlands.
Van den Bosch, M.J., Schreurs, P.J.G., and Geers, M G.D., 2006. An improved description of the exponential Xu and Needleman cohesive zone law for mixed-mode decohesion. *Engineering Fracture Mechanics*, 73, 1220–1234.
Van den Bosch, M.J., Schreurs, P.J.G., and Geers, M G.D., 2008. On the development of a 3D cohesive zone element in the presence of large deformations. *Computational Mechanics*, 42 (2), 171–180.
Xu, X.P., and Needleman, A, 1993. Void nucleation by inclusions debonding in a crystal matrix. *Modelling and Simulation in Materials Science and Engineering*, 1, 111–132.

Appendix A: Contact interface element resisting force

A.1. Introduction

The resisting force (internal force) due to the presence of contact interface elements is defined as:

$$\tilde{\mathbf{F}}_{\text{int}} = \int_{\Gamma} \mathbf{C}^{T}\mathbf{S}\,\tilde{\boldsymbol{\sigma}}_{el}\,d\Gamma + \int_{\Gamma} \mathbf{C}^{T}\mathbf{S}\,\tilde{\boldsymbol{\sigma}}_{c}\,d\Gamma \tag{A.1}$$

where Γ is the contact surface area, $\tilde{\boldsymbol{\sigma}}_{c}$ is the contact stress and $\tilde{\boldsymbol{\sigma}}_{el}$ is the elastic stress due to the presence of the contact element stiffness. The matrix $\mathbf{C}^{T}\mathbf{S}$ is defined in Eq. (A.1).

As discussed earlier in Section 2.4.3, the contact element stiffness is introduced to overcome the singularity of the global stiffness matrix. Because in reality contact interfaces do not have stiffness, any forces created due to the presence of this stiffness should not contribute to the force equilibrium equation. This concept will be shown for several contact states in the sections below.

A.2. Contact-free

This contact-free state occurs when bodies, which are not connected, are moving freely with respect to each other. It is a stress-free state, so no contact forces are occurring. Because of the introduced contact element stiffness, there will be the presence of an elastic stress $\tilde{\boldsymbol{\sigma}}_{el}$. The force created due to this stress is not physically existed (contact elements do not have stiffness) and therefore has to disappear from the force equilibrium equation.

To achieve this the contact stress correction vector $\Delta\mathbf{a}^{*}$ is set as:

$$\Delta\mathbf{a}^{*} = -{}_{i+1}\tilde{\boldsymbol{\sigma}}_{el} \tag{A.2}$$

where i is step number. Using this into the update of the contact stress vector ${}_{i+1}\tilde{\boldsymbol{\sigma}}_{c}$ gives:

$${}_{i+1}\tilde{\boldsymbol{\sigma}}_{c} = {}_{i}\tilde{\boldsymbol{\sigma}}_{c} + \Delta\mathbf{a}^{*} = {}_{i}\tilde{\boldsymbol{\sigma}}_{c} - {}_{i+1}\tilde{\boldsymbol{\sigma}}_{el} = -{}_{i+1}\tilde{\boldsymbol{\sigma}}_{el} \tag{A.3}$$

Here ${}_{i}\tilde{\boldsymbol{\sigma}}_{c}$ is zero, because there is no contact between the bodies.

The resisting force due to the presence of contact interface elements is now computed as:

$$\begin{aligned}\tilde{\mathbf{F}}_{\text{int}} &= \int_{V} \mathbf{C}^{\mathrm{T}}\mathbf{S}\,\tilde{\boldsymbol{\sigma}}_{el}\,dV + \int_{V} \mathbf{C}^{\mathrm{T}}\mathbf{S}\,\tilde{\boldsymbol{\sigma}}_{c}\,dV \\ &= \int_{V} \mathbf{C}^{\mathrm{T}}\mathbf{S}\,\tilde{\boldsymbol{\sigma}}_{el}\,dV - \int_{V} \mathbf{C}^{\mathrm{T}}\mathbf{S}\,{}_{i+1}\tilde{\boldsymbol{\sigma}}_{el}\,dV = \mathbf{0}\end{aligned} \tag{A.4}$$

A.3. debonding

This contact state occurs when two bodies, which were connected, are getting separated. Similarly as to the closing contact state, the 'unreal' elastic stress $\tilde{\boldsymbol{\sigma}}_{el}$ due to the introduced contact element stiffness should not have any effect in the force equilibrium equation.

In this case the contact stress correction vector $\Delta\mathbf{a}^{*}$ is set as:

$$\Delta\mathbf{a}^{*} = {}_{i+1}\mathbf{T} - {}_{i+1}\tilde{\boldsymbol{\sigma}}_{el} - {}_{i}\tilde{\boldsymbol{\sigma}}_{c} \tag{A.5}$$

where ${}_{i}\tilde{\boldsymbol{\sigma}}_{c}$ is the already present contact stress and $\mathbf{T}$is the stress due to the cohesive interface law.

Using this into the update of the contact stress vector ${}_{i+1}\tilde{\boldsymbol{\sigma}}_{c}$ gives:

$$\begin{aligned}{}_{i+1}\tilde{\boldsymbol{\sigma}}_{c} &= {}_{i}\tilde{\boldsymbol{\sigma}}_{c} + \Delta\mathbf{a}^{*} = {}_{i}\tilde{\boldsymbol{\sigma}}_{c} + ({}_{i+1}\mathbf{T} - {}_{i+1}\tilde{\boldsymbol{\sigma}}_{el} - {}_{i}\tilde{\boldsymbol{\sigma}}_{c}) \\ &= {}_{i+1}\mathbf{T} - {}_{i+1}\tilde{\boldsymbol{\sigma}}_{el}\end{aligned} \tag{A.6}$$

The resisting force due to the presence of contact interface elements is now computed as:

$$\begin{aligned}\tilde{\mathbf{F}}_{\text{int}} &= \int_{V} \mathbf{C}^{\mathrm{T}}\mathbf{S}\,{}_{i+1}\tilde{\boldsymbol{\sigma}}_{el}\,dV + \int_{V} \mathbf{C}^{\mathrm{T}}\mathbf{S}\,{}_{i+1}\tilde{\boldsymbol{\sigma}}_{c}\,dV = \\ &= \int_{V} \mathbf{C}^{\mathrm{T}}\mathbf{S}\,{}_{i+1}\tilde{\boldsymbol{\sigma}}_{el}\,dV + \int_{V} \mathbf{C}^{\mathrm{T}}\mathbf{S}\,({}_{i+1}\mathbf{T} - {}_{i+1}\tilde{\boldsymbol{\sigma}}_{el})\,dV = \int_{V} \mathbf{C}^{\mathrm{T}}\mathbf{S}\,{}_{i+1}\mathbf{T}\,dV\end{aligned} \tag{A.7}$$

From this equation it is clear that the presence of the 'unreal' elastic stress $\tilde{\boldsymbol{\sigma}}_{el}$ does not contribute to the resisting force of the contact interfaces.